Retrieval of Ocean Wave Heights from Spaceborne SAR over the Arctic Marginal Ice Zone with a Neural Network

Ke Wu[1], Xiaoming Li[2], and Bingqing Huang[3]

[1]Aerospace Information Research Institution, Chinese Academy of Sciences
[2]Aerospace Information Research Institute, Chinese Academy of Sciences (CAS)
[3]Aerospace Information Research Institute, Chinese Academy of Sciences

November 21, 2022

Abstract

The twin Sentinel-1 (S1) satellites have been extensively acquiring synthetic aperture radar (SAR) data in the Arctic, providing the unique opportunity to obtain ocean dynamic parameters with both high spatial resolution and wide swath coverage in the marginal ice zone (MIZ). In this paper, we proposed a method for retrieving the ocean significant wave height (SWH) from S1 SAR data in horizontal-horizontal (HH) polarization based on a backpropagation neural network (BPNN). A total of 4,273 scenes from S1 extra wide swath mode data acquired in the Arctic were collocated with data from four radar altimeters (RA), yielding 126,128 collocated data pairs. These data were separated into training and testing datasets to develop a BPNN model for retrieving SWH. Comparing the S1 retrieved SWH using the testing dataset with the RA SWH yielded a bias of 0.17 m, a root-mean-square error of 0.71 m and a scatter index of 23.05% for SWH less than 10 m. The S1 retrieved SWH were further compared with CFOSAT/SWIM data acquired in the Arctic between August 2019 and May 2020 to validate the SWIM performance on wave measurements at different beams.

Retrieval of Ocean Wave Heights from Spaceborne SAR over the Arctic Marginal Ice Zone with a Neural Network

Ke Wu[1,2], Xiao-Ming Li[2] and Bingqing Huang[1,2]

[1]University of Chinese Academy of Sciences, Beijing, 100049, China.

[2]Key Laboratory of Digital Earth Science, Aerospace Information Research Institute, Chinese Academy of Sciences, Beijing, 100094, China.

Corresponding author: Xiao-Ming Li (lixm@radi.ac.cn)

Key Points:

- An algorithm is developed to retrieve SWH in the Arctic marginal ice zone from spaceborne SAR using a back propagation neural network
- Comparisons of the SAR-retrieved SWH with radar altimeter data suggest good agreement independent of the sea state
- SWIM data at nadir and the 10° beam in the Arctic MIZ are validated in detail by the SAR-retrieved SWH

Abstract

The twin Sentinel-1 (S1) satellites have been extensively acquiring synthetic aperture radar (SAR) data in the Arctic, providing the unique opportunity to obtain ocean dynamic parameters with both high spatial resolution and wide swath coverage in the marginal ice zone (MIZ). In this paper, we proposed a method for retrieving the ocean significant wave height (SWH) from S1 SAR data in horizontal-horizontal (HH) polarization based on a backpropagation neural network (BPNN). A total of 4,273 scenes from S1 extra wide swath mode data acquired in the Arctic were collocated with data from four radar altimeters (RA), yielding 126,128 collocated data pairs. These data were separated into training and testing datasets to develop a BPNN model for retrieving SWH. Comparing the S1 retrieved SWH using the testing dataset with the RA SWH yielded a bias of 0.17 m, a root-mean-square error of 0.71 m and a scatter index of 23.05% for SWH less than 10 m. The S1 retrieved SWH were further compared with CFOSAT/SWIM data acquired in the Arctic between August 2019 and May 2020 to validate the SWIM performance on wave measurements at different beams.

Plain language summary

The rapid decline of sea ice in the Arctic creates wider marginal ice zone (a transit from open water to sea ice, MIZ) than ever. Some studies have suggested that interaction between ocean dynamics (e.g., sea surface wind and wave) and sea ice is one possible feedback to retreat of sea ice in the Arctic. Therefore, ocean wave data in the MIZ is highly desirable. Synthetic aperture radar, as an active remote sensing technique, can operate independent on sunlight and weather conditions and image the earth with high spatial resolution. However, due to the complicated imaging process of ocean waves by spaceborne SAR, retrieval of sea state parameters by SAR data has been investigated for decades. Here, we developed an algorithm based on a back propagation neural network to retrieve significant wave height from spaceborne SAR data. This provides a chance of obtaining wave height information in both large coverages and high spatial resolution from satellite observation, and therefore, can contribute to scientific study, offshore operation and shipping in the Arctic.

1 Introduction

Prior to the launch of the Chinese French Oceanic Satellite (CFOSAT) with its onboard Surface Waves Investigation and Monitoring (SWIM) sensor, the only sensor capable of imaging ocean waves in two dimensions from space was the spaceborne synthetic aperture radar (SAR), which provides images with high spatial resolution. The SAR imaging mechanism of ocean waves is complex which is generally explained by three modulations: tilt modulation, hydrodynamic modulation and velocity bunching (Valenzuela, 1978; Alpers et al., 1981). While tilt and hydrodynamic modulations are also shared by real-aperture radar as the dominant imaging mechanisms of ocean waves, velocity bunching is unique for SAR to image ocean waves. The moving scatterer of water particles with a velocity either towards or away from a moving SAR sensor, causes an azimuthal shift in SAR images. In addition, velocity bunching in the SAR resolution cell leads to an azimuth cut-off, that is, the minimum

SAR-detectable wavelength of ocean waves traveling in the azimuth direction. Therefore, the nonlinearity of SAR ocean wave imaging complicates their retrieval. In the following, we briefly summarize the existing methods used to retrieve ocean wave information in terms of both two-dimensional spectrum and integral wave parameters.

The Max Planck Institute (MPI) scheme developed by (Hasselmann & Hasselmann, 1991; Hasselmann et al., 1996) is the widely used method to retrieve two-dimensional ocean wave spectra from spaceborne SAR data. The MPI method iteratively searches for the minimum of cost function to retrieve wave spectra from SAR by using a numerical ocean wave model (e.g., the WAM model) for the first-guess wave spectra. These first-guess wave spectra provide the wave propagation direction and compensate for the loss of wave information in high-frequency during the SAR imaging process. By this way, nonlinear retrievals can get the complete two-dimensional spectra of ocean waves. Therefore, these methods strongly depend on the first-guess wave spectra as prior information. Alternatively, wind vectors measured by a scatterometer can be utilized to estimate generally missed windsea information by SAR imaging ocean waves, e.g., the semi parametric retrieval algorithm scheme (SPRA) developed by Mastenbroek & De Valk (2000), which also applies full nonlinear mapping relations between ocean waves and SAR imaging. The SPRA combines the observed SAR spectrum with collocated scatterometer wind vectors to estimate the windsea spectrum, while the residual signal in the SAR spectrum is considered as the swell. The SAR image spectra employed by the abovementioned methods are derived from intensity image. Alternatively, the partition rescaling and shift algorithm (PARSA) developed by Schulz-Stellenfleth et al. (2005) inputs the cross spectra derived from single-look-complex SAR data to a nonlinear inversion. This type of nonlinear retrieval methods can generally yield two-dimensional ocean wave spectra, enabling the derivation of integral ocean wave parameters, e.g., the significant wave height (SWH) and mean wave period. Nevertheless, due to their dependency on prior information, these methods inconvenient for wide applications as ocean wave model spectra are generally not publicly available. Moreover, nonlinear retrievals can be degraded to quasi-linear retrievals. By inputting the cross spectrum which resolves the ambiguity of ocean wave propagation in the quasi-linear retrieval (Engen & Johnsen, 1995), one can generally obtain ocean swell spectrum. The advantage of this approach is that prior information is no longer needed. Even though quasi-linear retrievals cannot yield full two-dimensional ocean wave spectra, the obtained swell spectra are particularly important for studying swell propagation and decay (Li, 2016; Ardhuin et al., 2019).

With the advantage of no prior information needed as input for retrievals, empirical algorithms for deriving integral ocean wave parameters by spaceborne SAR data are more practical than conventional nonlinear retrieval methods. Starting with CWAVE_ERS (Schulz-Stellenfleth et al., 2007), a few similar algorithms applied to C-band SAR data have been proposed, such as CWAVE_ENV (Li et al., 2011) and CWAVE_S1 (Stopa & Mouche, 2017). The general idea of these CWAVE-type algorithms is to establish empirical relations (e.g., polynomial fitting) between SAR image parameters and integral ocean wave parameters.

Compared with theoretical-based methods, these empirical type methods can yield full sea state (both wind wave and swell wave) parameters without conducting complicated nonlinear retrievals. Therefore, first-guess spectral information is no longer needed. Furthermore, although they are called empirical algorithms, the input parameters are not chosen randomly. For instance, the SAR normalized radar cross section (NRCS) and the corresponding image spectra, which are often used in empirical algorithms, form the basis of traditional nonlinear SAR ocean wave retrievals. Moreover, CWAVE-type algorithms attempt to incorporate the nonlinear relations among SAR images and ocean wave parameters using 2nd-order polynomials by cross-multiplying the input parameters. However, the nonlinear relationships between SAR image and ocean wave parameters are often too complex to be sufficiently represented by a 2nd-order polynomial. Therefore, the backpropagation neural network (BPNN), which has the ability to fit nonlinear relationships, has been employed to retrieve the SWH from SAR images and to improve the retrieval accuracy.

BPNN, a traditional machine learning method proposed in the 1980s (Rumelhart et al., 1986), has been shown to be effective at fitting nonlinear problems between input and output parameters. BPNN considers an iteration as the combination between the forward transmission of information and the backward transmission of error. The network is trained iteratively until the global error satisfies the preset accuracy or until the number of training iterations exceeds the specified maximum number of learning iterations. BPNN consists of an input layer, one or multiple hidden layers and an output layer. The input and output layers comprise the input and output data of the model, respectively. The hidden layer, which is not visible to users, is the key to fitting the relationship between the input and the output data. Stopa and Mouche (2017) used the BPNN model to retrieve SWH from Sentinel-1 (S1) wave mode (WV) data. In addition to BPNN, other machine learning methods have been used to retrieve wave parameters from SAR data; examples include the support vector machine (SVM) with the same parameters as CWAVE-type models (Gao et al., 2018), the extreme learning machine (ELM) with the wind speed as an input parameter (Kumar et al., 2018), the decision tree and the random forest algorithms (Shao et al., 2019) with the NRCS, incidence angle, azimuth angle and whole image spectrum as input parameters, and the convolutional neural network (CNN) (Xue et al., 2018) with the SAR sub-images as input of SAR sub-images.

The retrieval of wave parameters has great significance for studying the interaction between sea ice and sea waves in the marginal ice zone (MIZ), where the sea ice concentration is between 15% and 80%. The rate of decline in the seasonal Arctic sea ice extent accelerates continuously in recent years (Cavalieri & Parkinson, 2012; Comiso et al., 2017), leading to an expansion of the MIZ in summer (Strong & Rigor, 2013). This expansion of the MIZ provides space for ocean waves to grow and propagate. Research has shown an increase in ocean wave heights in the Arctic MIZ (Thomson & Rogers, 2014). Moreover, sea ice can fracture, overlap and accumulate under the dynamic effects of ocean waves (Asplin et al., 2012). Therefore, the interaction between ocean waves and sea ice has attracted considerable attention (Stopa et al., 2018; Nose et al., 2020). To date, most available ocean wave remote sensing products in the Arctic have been obtained by radar altimeter (RA). Besides, the CFOSAT, which was launched in 2018, can provide ocean wave spectra by the onboard SWIM sensor, which provides SWH data with pixel size of 18 km × 18 km at nadir beam and 70 km × 90 km at the 10° beam.

However, with the shortcoming of small coverage on account of nadir measurements of RAs and the coarse resolution of CFOSAT/SWIM, limited ocean wave products are available in the Arctic MIZ with both high spatial resolution and large coverage for studying the interaction between ocean waves and sea ice. The Copernicus Sentinel-1A (S1A) and Sentinel-1B (S1B) satellites have been in orbit since April 2014 and April 2016, respectively. This constellation significantly reduces the revisit period, thereby yielding a high temporal resolution, particularly in the polar regions. Approximately 3,000 S1 images are acquired every month in the Arctic, and most of the Arctic can be covered within two days. The twins have extensively acquired data in extra-wide (EW) swath mode and interferometric wide (IW) swath mode in the Arctic. Fig. 1 presents an example of the spatial coverages of the EW data acquired by S1A and S1B within six days in 2019. Additionally, the EW and IW data acquired in the Arctic are generally in polarization combination of co-polarization and cross-polarization, dedicated for sea ice monitoring (e.g., Hong & Yang, 2018; Soldal et al., 2019; Li et al., 2020). With a spatial resolution of 40 m, S1 EW images can generally yield good observations of ocean waves, as illustrated in Fig. 2. In the context of these advantages, the motivation of this study is to develop an algorithm dedicated for retrieving SWH in the Arctic using S1 data in HH polarization. These data certainly are useful for studying the interaction between sea ice and ocean dynamics, as both sea ice and marine-meteo parameters can be derived from SAR simultaneously.

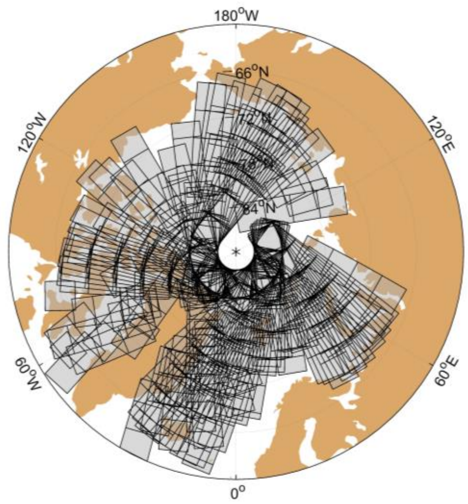

Figure 1. The coverage of S1 EW GRD data in HH polarization from 1 April to 6 April 2019.

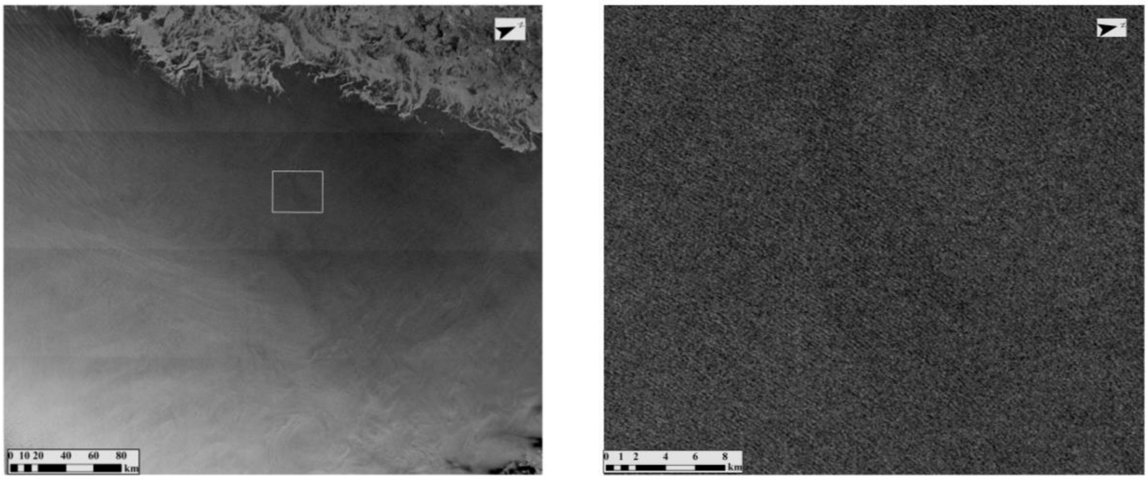

(a) (b)

Figure 2. (a) EW image in HH polarization acquired by S1B at 10:17 UTC on 28 January 2017 in the Davis Strait. The top of the image shows sea ice cover. (b) Sub-image (with a size of 900 × 750 pixels, approximately 36 × 30 km, corresponding to the area marked by the white square in (a)) showing ocean wave (swell) patterns. The image ID is S1B_EW_GRDM_1SDH_20170128T101704_20170128T101804_004047_006FF5_9AA4.

Following the introduction, the datasets used in this study are introduced in Section 2. Section 3 presents the methodology, including the data collocation and the development of the BPNN model to retrieve SWH by S1 EW data in HH polarization. Verification of the BPNN model for retrievals are shown in Section 4. In Section 5, a detailed comparison between the S1 retrieved SWH and the collocated CFOSAT/SWIM data is presented. A summary and the conclusions are given in the last section.

2 Datasets

2.1 S1A and S1B EW data

Most S1A and S1B EW data acquired in the Arctic are in dual-polarization (HH and HV). In this study, S1 Level-1 ground range detected (GRD) data in HH polarization are used to retrieve SWH. S1 EW images have a swath width of 400 km with a spatial resolution of 40 m. The radar incidence angle of the EW data ranges from 18.9° in the near range to 47.0° in the far range. Radiometric calibration and thermal noise removal of the EW data are conducted according to the S1 user manual (ESA, 2016). The NRCS σ_0 is obtained by:

$$\sigma_0 = \frac{DN^2 - n}{k_s^2} \#(1)$$

where DN is the digital number read from the tiff data file, n is the noise vector, and k_s is the calibration factor. The noise vector and calibration factor are given in the product noise and calibration metadata.

The EW GRD data used herein span the period between January 2017 and October 2019, comprising approximately 113,500 images.

As most of the S1 EW and IW data acquired over in situ buoys are in VV polarization, we found only 305 pairs of S1 data and National Data Buoy Center (NDBC) buoy data in the period from October 2014 to October 2019 (Li et al., 2020). Therefore, in this study, we used RA measurements of SWH in the Arctic as ground truth to develop the BPNN model.

2.2 RA SWH data

The RA SWH data are from four missions: CryoSat-2, Jason-2, Jason-3 and SARAL. These RA-measured SWH are screened, and only good quality data are retained. The CryoSat-2 data are provided by the European Space Agency (ESA, http://science-pds.cryosat.esa.int/) and can reach latitudes of 88°N. We used pole-to-pole Level-2 CryoSat-2 data with a 1 Hz sampling frequency and extracted the data with values for ‘*surf_type*’ of 0 (ocean) and ‘*flag_instr_op_mode*’ of 1 (good quality). Jason-2, Jason-3 and SARAL are all provided by the European Organization for the Exploitation of Meteorological Satellites (EUMETSAT, https://archive.eumetsat.int/usc/). While the Jason-2 and Jason-3 missions can reach latitudes of only 66.15°, SARAL can cover more of the Arctic, up to 81.49°N. We extracted the data of these three RA missions with values for ‘*surface_type*’ of 0 (ocean) and ‘*qual_swh*’ of 0 (good quality).

Prior to using the RA data from the four missions above to construct the BPNN model, we conducted cross-comparisons among the four RA missions. The RA missions in each pair were matched with temporal interval less than 1 hour and spatial distance less than 10 km for cross-comparisons in the region above 60°N. The corresponding statistical parameters of these comparisons are listed in Table 1. The twin satellites, Jason-2 and Jason-3, achieve the best agreement with a bias of 0.04 m and a root-mean-square error (RMSE) of 0.00 m. The comparisons between CryoSat-2 and Jason-2/3 also show good compatibility with biases of -0.01/-0.02 m and RMSEs of 0.02/0.01 m. The differences between CryoSat-2 and SARAL and between Jason-3 and SARAL are slightly higher with biases of -0.06 m and 0.06 m, respectively, but the RMSEs of these two comparisons are only 0.01 m and 0.02 m, respectively. Therefore, the discrepancies among the SWH data from these four RA missions are minor, and we did not calibrate the data based on data from a single RA mission.

Table 1. Cross-comparisons among the SWH data from the four RA missions between January 2017 and October 2019 across the pan-Arctic.

	Jason-2		Jason-3		SARAL	
	Bias/m	RMSE/m	Bias/m	RMSE/m	Bias/m	RMSE/m
CryoSat-2	-0.01	0.02	-0.02	0.01	-0.06	0.01
Jason-2	/	/	0.04	0.00	0.00	0.02
Jason-3	/	/	/	/	0.06	0.02

2.3 CFOSAT

CFOSAT was launched on 29 October 2018 carrying a real-aperture scanning radar, SWIM. In addition to the wave sensor, CFOSAT also carries a scatterometer to measure sea surface winds (Liu et al., 2020). The SWIM sensor scans the sea surface by 6 rotating beams at small incidence angles of 0°, 2°, 4°, 6°, 8° and 10°. For its nadir measurements, SWIM can be regarded as an RA providing SWH, while the off-nadir beams at 6°, 8° and 10° provide directional wave spectra and the corresponding integral ocean wave parameters.

A preliminary analysis of the SWIM data quality in comparison with Jason-3 and SARAL showed that the SWIM nadir SWH were slightly lower than the RA SWH by 0.01 m and 0.06 m, respectively (Hauser et al., 2020). With respect to the quality of wave data acquired at different beams (except at nadir) by SWIM, Hauser et al. (2020) suggested that the data acquired at 10° have the best quality compared with the data acquired at other beams. Therefore, we used the SWIM sea state data obtained at nadir and 10° beam to compare with the S1 retrieved SWH. The SWIM products were operationally provided for use on 28 July 2019; accordingly, the SWIM Level-2 data employed in this study range from August 2019 to May 2020. The nadir beam of SWIM Level-2 data provides NRCS profiles, SWH and wind speed values using a new retracking algorithm (Hauser et al., 2020). The 10° beam provides two-dimensional wave spectra, which include 12 directions from 0° to 180° (with a 180° directional ambiguity) and 65 wave number bins from 0.0046 rad/m to 0.2770 rad/m (corresponding to wavelengths from approximately 70 m to 500 m). Each spectrum represents the average sea state in a large area covering 70 × 90 km. Integral wave parameters in terms of the SWH, dominant wave direction and dominant wavelength are also provided in SWIM Level-2 data.

3 Methodology

3.1 Collocation of the S1 EW and RA data

The S1 EW scenes were collocated with the RA data with a temporal window of less than 90 minutes. A total of 4,273 S1 EW scenes were collocated with the data from the four RA missions, among which 1,834 and 2,439 scenes were acquired by S1A and S1B, respectively. The spatial distributions of the collocated S1A and S1B EW images are presented in Fig. 3. Then, the S1 EW sub-images with dimensions of 256 × 256 pixels (i.e., 10,240 m×10,240 m) collocated with the RA footprints were collected as matchups. Finally, a total of 153,485 collocation data pairs of S1 and RA data between January 2017 and October 2019 were obtained.

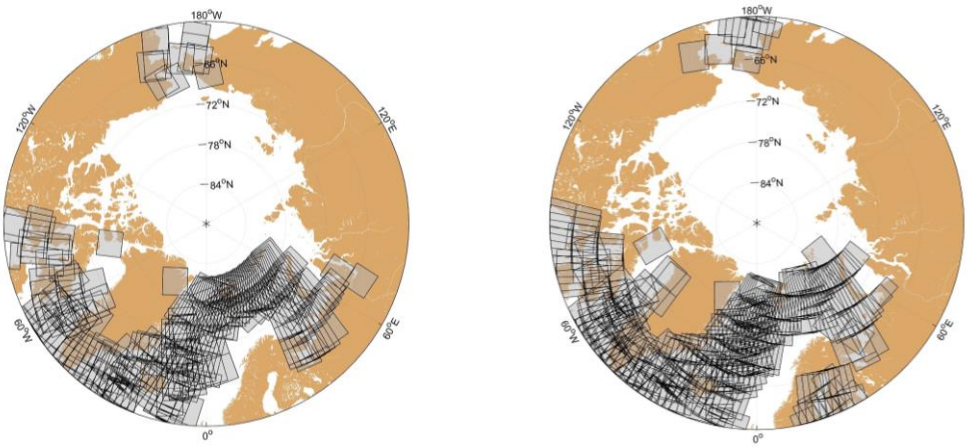

(a) (b)

Figure 3. Spatial distributions of (a) S1A and (b) S1B images collocated with the RA data in the period between January 2017 and October 2019.

As a large amount of S1 EW data were acquired in the Arctic MIZ, they often present a mixture of sea ice and open water. Therefore, we used the reanalysis daily sea ice cover product (with a grid size of 1 km) of the ice mapping system (IMS) to filter out ice-covered sub-images.

In addition, the quality of the S1 sub-images has a significant impact on the SWH retrievals. We used the homogeneity parameter (Schulz-Stellenfleth & Lehner, 2004) to filter out S1 sub-images on presenting some oceanic and atmospheric features not related to ocean surface waves. On the other hand, the IMS data are daily products and have discrepancies with the S1 observations, which are snapshots. Therefore, a homogeneity test can also discard sub-images presenting sea ice features (particularly pancake and icebergs (Lehner & Ocampo-Torres, 2003)) not identified by the IMS data. The homogeneity parameter ξ_H is defined in (2):

$$\xi_H = \left(\sum_k \overline{mean}(\widehat{\Phi}_k)\right)^{-1} \sum_k \frac{\overline{var}(\widehat{\Phi}_k)}{\overline{mean}(\widehat{\Phi}_k)} \#(2)$$

where $\widehat{\Phi}_k$ is the power spectral density of each sub-image. Generally, the sea surface is considered homogeneous for ξ_H<1.05. The statistics of the homogeneity values are shown in Fig. 4.

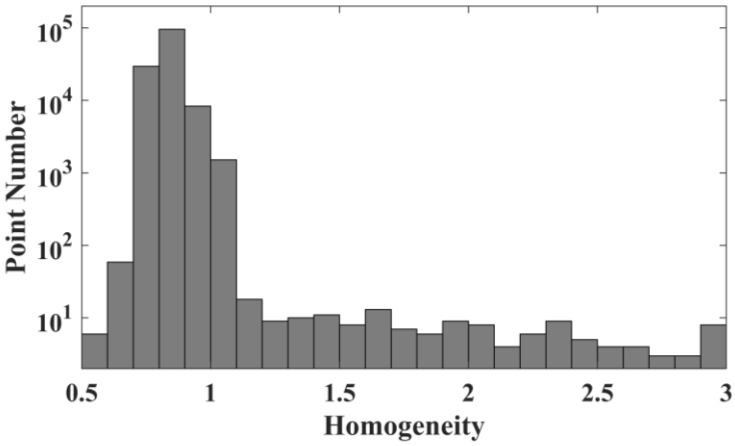

Figure 4. Histogram of homogeneity values for the 153,485 S1 sub-images collocated with data from four RA missions. The homogeneity values in the range from 0.5 to 3 are shown.

Furthermore, RA-measured SWH less than 0.5 m were excluded from the collocations considering the limitation on the RA measurement accuracy and the increased noise of SAR signals in low sea states (Ulaby et al., 2015). Finally, a total of 126,128 collocated data were obtained for use in this study. The numbers of collocation data pairs of S1 with different RA missions are listed in Table 2.

Table 2. Number of collocations between the S1 SWH and the data from the four RA missions between January 2017 and October 2019.

Radar Altimeters	Number of Collocations
CryoSat-2	37,674
Jason-2	34,657
Jason-3	45,791
SARAL	8,006
Total	126,128

3.2 Extraction of S1 image parameters

CWAVE-type empirical models have been developed for ERS/SAR, ENVISAT/ASAR and S1/SAR WV data. Recently, we have finished processing the ten-year WV dataset of ENVISAT/ASAR to obtain the sea state parameters based on the CWAVE_ENV model, and the results suggest good agreements with in situ buoy data and RA data (Li & Huang, 2020). Therefore, we also chose parameters similar to those used in CWAVE-type algorithms to retrieve SWH by the S1 data: the mean NRCS (denoted $\bar{\sigma}_0$), normalized image variance (cvar), and 20 spectral parameters computed from the variance spectrum of a sub-image. The $\bar{\sigma}_0$ and cvar are computed as follows:

$$\bar{\sigma}_0 = \langle \sigma_0 \rangle \#(3)$$

$$cvar = var\left(\frac{I - \langle I \rangle}{\langle I \rangle}\right) \#(4)$$

where $\langle I \rangle$ is the mean intensity of an S1 sub-image.

The 20 spectral parameters are extracted from the SAR image spectrum using a set of orthonormal functions. The SAR image spectrum is estimated by computing the image periodogram with a two-dimensional fast Fourier transform (FFT) algorithm. These orthonormal functions can extract the features of the image spectrum from 20 different directions. The method for extracting the 20 SAR image spectral parameters is described in detail in the Appendix.

The previously developed CWAVE-type algorithms for SAR WV data do not include the parameter of incidence angle, as WV data have fixed incidence angles of approximately 23° for ERS/SAR and ENVISAT/ASAR WM data or angles of 23° and 33° for S1 WV data. However, S1 EW mode data have incidence angles ranging from 19° to 47°, while the NRCS significantly varies with the incidence angle. Therefore, the incidence angle θ should be included as a key input parameter to the neural network. Previous studies on developing empirical methods for SWH retrieval by SAR data used different forms of incidence angles, such as $\tan\theta$(Bruck & Lehner, 2013), $\cos\theta^2$(Ding et al., 2019) and θ(Pramudya et al., 2019; Shao et al., 2019). We had tried the $\sin\theta$, $\cos\theta$, $\tan\theta$ and θ(in units of radians) to input into the neural network. It is found that inputting $\cos\theta$ into the neural network achieved the best retrieval results while had slightly difference from inputting the other expressions of θ. Thus, 23 parameters, i.e., the mean NRCS, *cvar*, $\cos\theta$ and 20 spectral parameters, are collected in an input vector in the proposed BPNN model, which is denoted as X:

$$X = (\bar{\sigma}_0, cvar, \cos\theta, S_1, \dots, S_{20})^T \#(5)$$

3.3 Technical specifications of the proposed BPNN model

The designed BPNN model consists of an input layer, four hidden layers and an output layer; the structure is depicted in Fig. 5. The input vector X including 23 parameters as described in subsection 3.2 is used as the input layer, and the collocated RA SWH is the output layer. The numbers of nodes in the four hidden layers are 30, 20, 10 and 5, respectively.

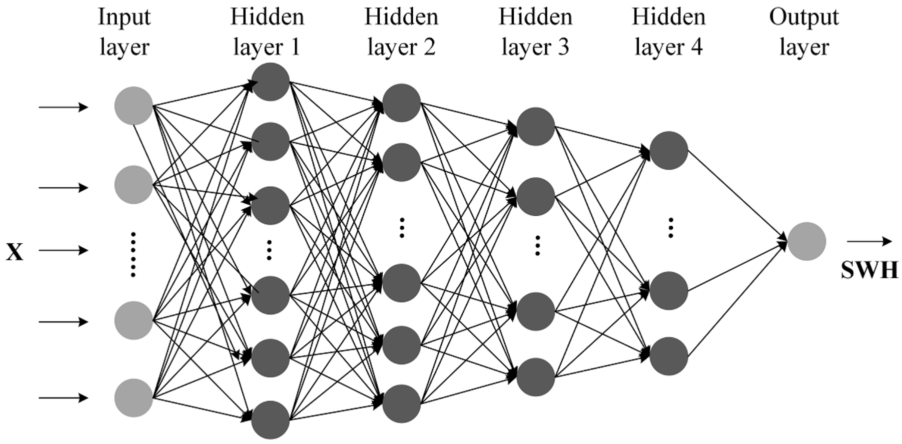

Figure 5. Structure of the proposed BPNN model for retrieving SWH from S1 data.

The function of each node in the network is to calculate the scalar product of the input vector X and weight vector W using a nonlinear transfer function. This nonlinear transfer function, called the activation function, is the key to improving the approximation ability of a neural network and is expressed as follows:

$$net_j = W_j^T X + b_j \#(6)$$

$$y_j = f\left(W_j^T X + b_j\right) = f\left(net_j\right) \#(7)$$

where the activation value of node *j* is net_j, W_j is the connection weight vector from the nodes of the upper layer to node *j* of this layer, b_j represents the bias of node *j*, y_i is the output of node *j*, and $f(\cdot)$ is the activation function of a node. The activation function of the second hidden layer is a sigmoid function (we used *logsig*), and the activation function of the other hidden layers is the hyperbolic tangent function (*tansig*); these two functions are given in (8) and (9), respectively. The activation function of the output layer is "*purelin*", a linear transfer function. Fig. 6 illustrates these activation functions, in which the x-axis and y-axis are the input and output of the nodes, respectively, and the solid line represents their relationship.

$$logsig = \frac{1}{1 + e^{-x}} \#(8)$$

$$tansig = \frac{e^{x} - e^{-x}}{e^{x} + e^{-x}} \#(9)$$

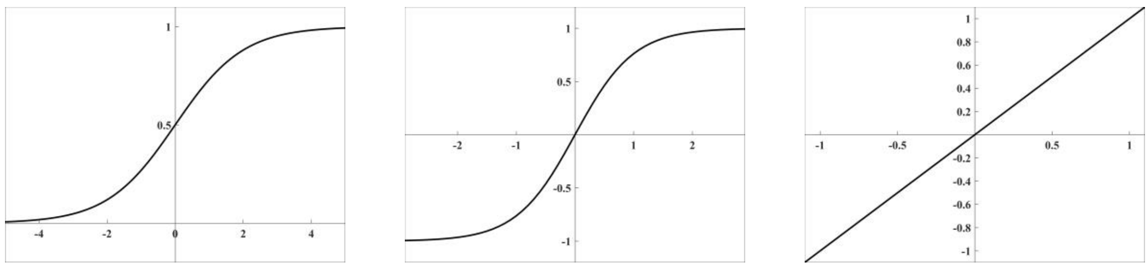

(a) (b) (c)

Figure 6. Plots of the (a) *logsig*, (b) *tansig*, and (c) *purelin* activation functions used in the BPNN model. The x-axis and y-axis represent the input and the output values of the nodes, respectively.

After forward-propagating the data in the input layer to the hidden layers, the network computes the result O in the output layer. A global error E is computed based on the performance function of the mean square error (MSE), which is given as follows:

$$E = \frac{1}{n}\sum_{n}(O_1 - R_t)^2 \#(10)$$

$$O = f_o\left(\sum_{j} w_{oj}y_j + b_o\right)\#(11)$$

where w_{oj} is the connection weight from the hidden node j to the output node o, b_o is the bias of the output node o, $f_o(\cdot)$ is the activation function of the output layer node, and R_t is the true value of the training data. The global error E is one of the parameters used to determine whether the iteration terminates; E is also used to update the weight of each layer according to the training function and the learning rate. In this model, we use "*trainbfgs*" (BFGS quasi-Newton method) as the training function because this function can avoid computing the second derivative and the inverse of the Hesse matrix to increase the computational efficiency. The learning rate is set to 0.5. The network is trained iteratively until the global error meets the preset accuracy or the number of training iterations exceeds the specified maximum number of learning iterations.

To find an appropriate combination of the number of hidden layers and the number of nodes in each hidden layer, we conducted many experiments until the retrieval results showed the best agreement with the collocated RA SWH data based on three statistical parameters: the bias, RMSE and scatter index (SI). The tested number of hidden layers ranged from 2 to 5, and the number of nodes changed according to the number of hidden layers. In our study, the number of input parameters greatly exceeds that in other applications using BPNN, resulting in more hidden layers and nodes.

4 Training and verification of the BPNN model to retrieve SWH from S1 EW data

Seventy percent of the collocated S1 and RA data pairs are used as the training data (94,596 collocations) to train the BPNN model, and the remaining pairs (31,532 collocations) compose the testing data. The 23 input parameters and the output parameter (SWH) are normalized using equation (12), which can significantly improve the convergence rate of the BPNN:

$$X_i = \frac{x_i - x_{min}}{x_{max} - x_{min}}\#(12)$$

where x_i represents either the input or the output parameters, x_{min} and x_{max} are the minimum and maximum values of each parameter, respectively, and X_i represents the normalized input and output data. After normalization, the input and output parameters are between 0 and 1. To use the proposed BPNN model to retrieve SWH from S1 EW data, the output data should be anti-normalized to practical values.

Three parameters are assigned as termination conditions. The maximum number of iterations is set to 5,000, and the minimum of MSE is set to 0.001. The maximum failure time is set to 6, where failure is defined when the global error in the current iteration is larger than that in the previous iteration.

After training the BPNN model, three statistical parameters, namely, the bias, RMSE and SI, are used to evaluate the comparisons between the S1 retrieved SWH using BPNN and the RA SWH. The three parameters are computed as follows:

$$Bias = \bar{Y} - \bar{X}\#(13)$$

$$RMSE = \sqrt{\frac{1}{N}\sum (Y_i - X_i)^2}\#(14)$$

$$SI = \frac{1}{\overline{X_i}}\sqrt{\frac{1}{N}\sum \left[\left(Y_i - \bar{Y}\right) - \left(X_i - \bar{X}\right)\right]^2}\#(15)$$

where Y is the S1 retrieved SWH and X is the RA SWH.

Fig. 7 (a) and (b) show comparisons between the S1 retrieved SWH and RA SWH using the training and testing datasets, respectively. With respect to the comparison using the training dataset, the bias of 0.02 m, the RMSE of 0.62 m and the SI of 20.67% show that the S1 retrieved SWH is close to the RA SWH. The comparison using the testing dataset achieves almost identical statistical parameters with a bias of 0.02 m, an RMSE of 0.63 m and an SI of 21.07%. This finding indicates that the trained BPNN model has stable performance on the SWH retrieval from S1 EW data. However, these comparisons suggest that the retrieved SWH is lower than the RA SWH when the SWH exceeds 4 m, as indicated by the error bars in Fig. 7. Moreover, the underestimation increases with SWH increasing.

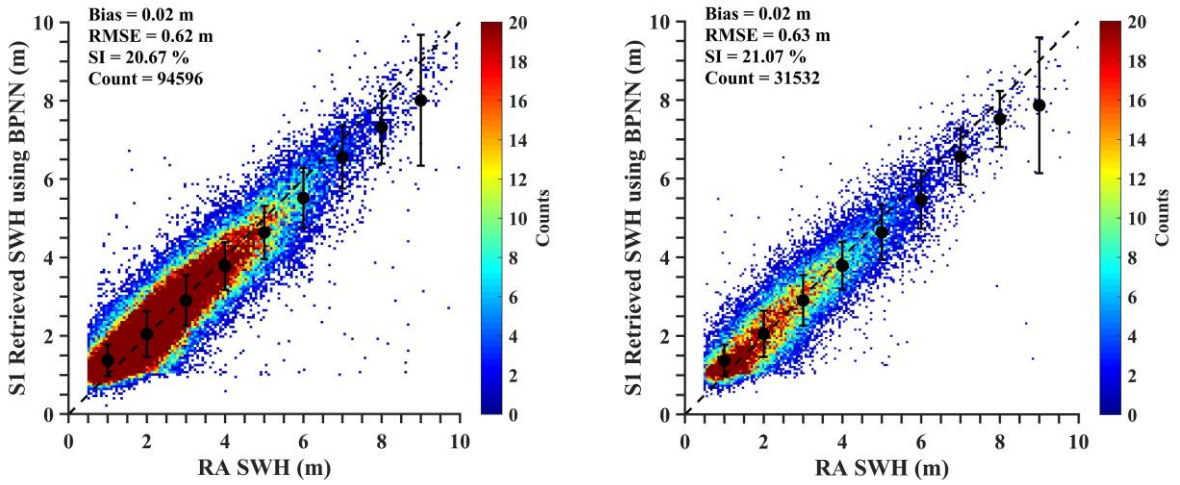

(a) (b)

Figure 7. Comparisons between the S1 retrieved SWH and RA SWH using (a) the training dataset and the (b) testing dataset.

A method of duplicating training data in high sea state is used to solve the underestimation afflicting the S1 retrieved SWH. Fig. 8 (a) shows a histogram of the RA SWH in the training dataset suggesting that the amount of data in high sea state is far less than the amount of data in low to moderate sea state, e.g., between 2 and 4 m. This is likely a major cause of the underestimation of S1 retrieved SWH in high sea state. To solve this problem, we arbitrarily changed the distribution of the training dataset to normal distribution (as shown in Fig. 8 (b)) by discarding some training samples with SWH lower than 3.3 m and duplicating samples with SWH higher than 3.3 m, resulting in another training dataset with 153,691 data pairs. We retained the original testing data to verify the training of the network, which histogram is shown in Fig. 8 (c).

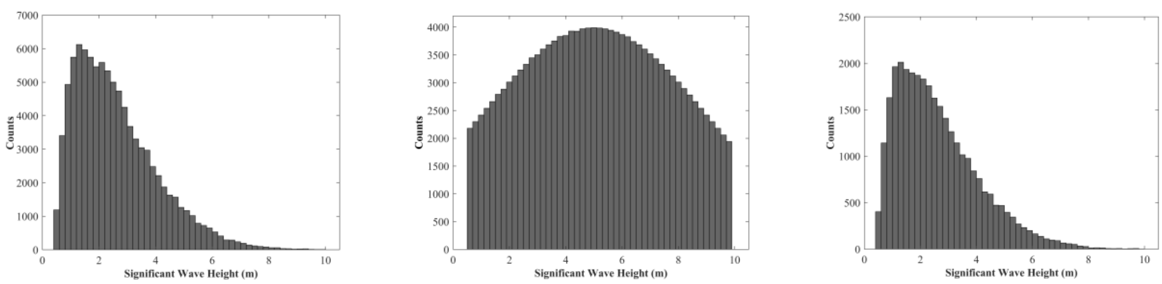

(a) (b) (c)

Figure 8. Histograms for the collocated RA SWH of (a) the original training dataset, (b) the adjusted training dataset by duplicating samples in high sea states, and (c) the testing dataset.

The BPNN was re-trained by using the adjusted training dataset and the retrievals using the new network were compared with the RA data, as shown in Fig. 9. Fig. 9 (a) shows the comparison using the full training dataset (including the duplicated cases in high sea state), and Fig. 9 (b) presents the comparison without including the duplicated cases. Both (a) and (b) suggest that the underestimation of SAR retrievals is effectively resolved using the adjusted training dataset. By comparing Fig. 9 (a) with Fig. 9 (b), one can refer to the effect of those duplicated cases in high sea state in the BPNN training. By excluding the duplicated data from the comparison, all three parameters increase accordingly. The comparison based on the training dataset without duplicating (Fig. 9 (b)) reveals statistical parameters that are almost identical to those of the comparison using the testing dataset with a bias of 0.17 m, an RMSE of 0.71 m and an SI of 23.05%, as shown in Fig. 9 (c). However, these statistics parameters are higher than those achieved using the original training dataset (Fig. 7 (b)). Therefore, we resolved the underestimation of SAR retrievals from moderate to high sea states but at the cost of increasing the overall statistical parameters.

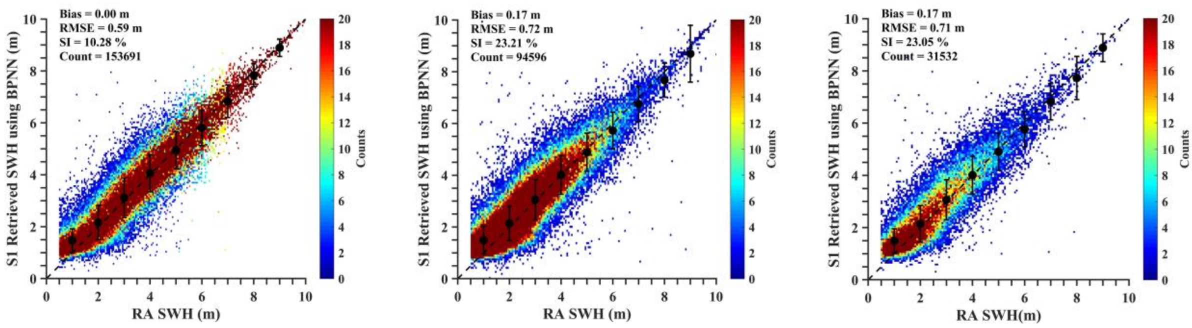

(a) (b) (c)

Figure 9. Comparisons between the S1 retrieved SWH and RA SWH using (a) the training dataset after duplicating, (b) the original training dataset and (c) the testing dataset.

In the following, we present two cases to demonstrate the advantages of sea state observations by S1 in the Arctic MIZ based on the proposed method. The first case is in the east of Greenland; the S1A EW data were acquired at 19:15 UTC on 6 December 2018. The retrieved SWH using the developed BPNN model is shown in Fig. 10 (a). Fig. 10 (c) presents the corresponding ERA-5 reanalysis wind field at 19:00 UTC on 6 December 2018, showing a cyclone weather situation with wind speeds above 20 m/s in the northwest of the S1 SWH map leading the SWH to exceed 6 m therein. The overlaid track in Fig. 10 (a) is the collocated CryoSat-2 SWH measurements from 18:45 to 18:46 UTC. The collocated S1 retrievals (triangles) with the Cryosat-2 SWH (circles) along the track are shown in Fig. 10 (e). From this scatter diagram, the S1 SWH is close to the CryoSat-2 SWH, especially between the latitude of 61°N to 62.5°N, where the difference between the S1 SWH and CryoSat-2 SWH is only 0.10 m. The S1 retrievals are slightly lower than the CryoSat-2 SWH south of 61°N (lower by 0.93 m on average) but are higher than the CryoSat-2 SWH north of 62.5°N (where the sea state is generally above 7 m) with significant spatial variation.

The second case is also in the east of Greenland but the data were acquired by S1B at 08:13 UTC on 28 November 2018. The S1 retrieved SWH is shown in Fig. 10 (b), in which the gray area represents the coverage of sea ice (extracted from the IMS data). Fig. 10 (d) presents the ERA-5 reanalysis sea surface wind field at 08:00 UTC on 28 November 2018.

The case shows a strong wind above 15 m/s blowing from the northeast to the southwest, and as a result, the SWH increases from northeast to southwest. The overlaid track represents the measurements of Jason-3 from 09:12 to 09:13 UTC on 28 November 2018, which is approximately 1 hour later than the S1B sensing time. The collocated S1 retrievals (triangles) with the Jason-3 SWH (circles) along the track are shown in Fig. 10 (f). In according with the Jason-3 SWH, the S1 SWH decreases with the increasing of latitude, as shown both in the scatter diagram (Fig. 10 (f)) and in the SWH map (Fig. 10 (d)). The S1 retrievals are slightly higher than the Jason-3 SWH south of 65.35°N and between 65.55°N and 65.6°N, where the mean absolute deviation is 1.41 m and 0.96 m, respectively.

The both cases were selected under the condition of significant spatial variation of sea state in the Arctic MIZ. While the RAs yield accurate measurements of SWH along satellite tracks, the advantage of spaceborne SAR is that it can map sea state variations over a large coverage and in a high spatial resolution.

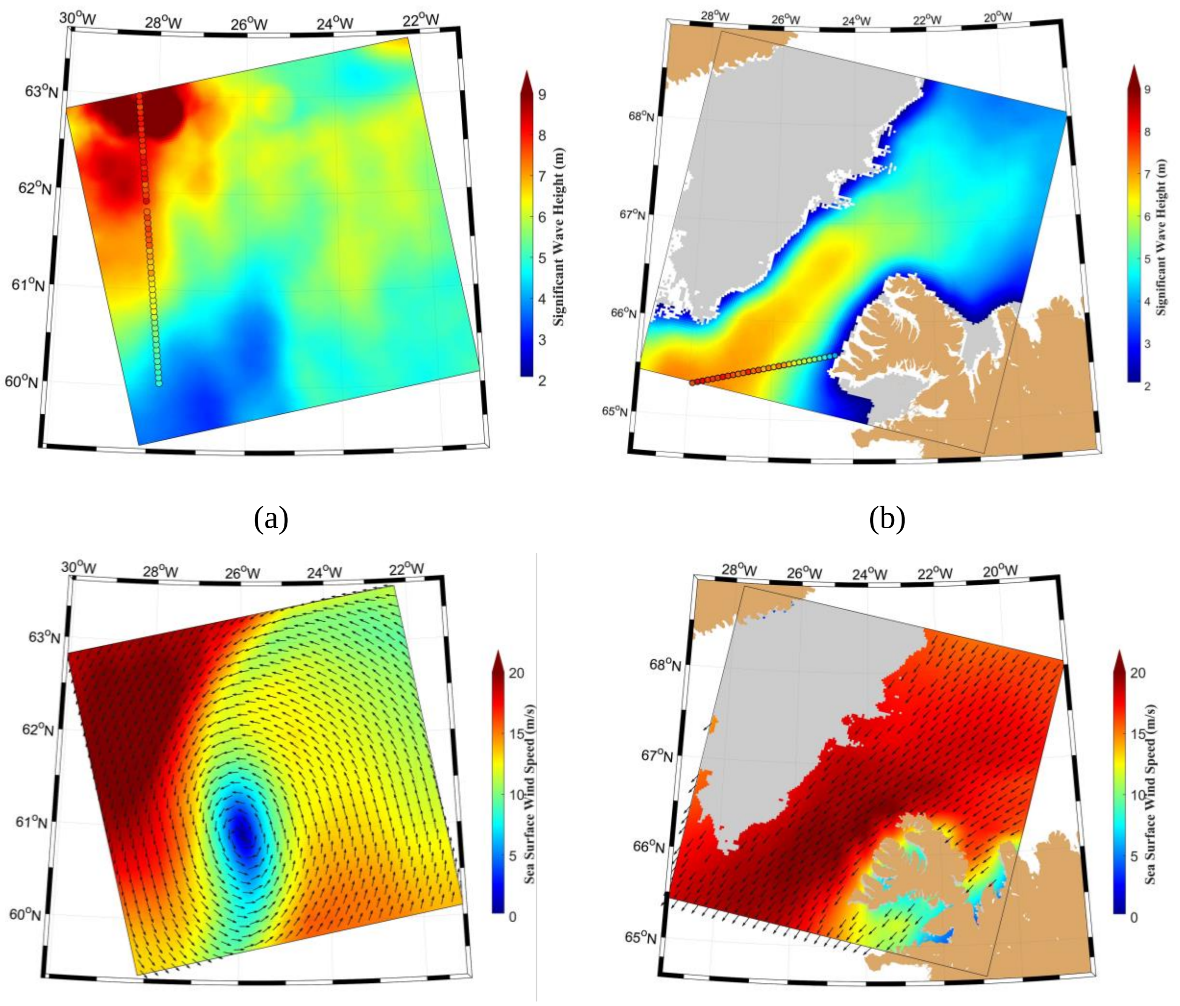

(a) (b)

(c) (d)

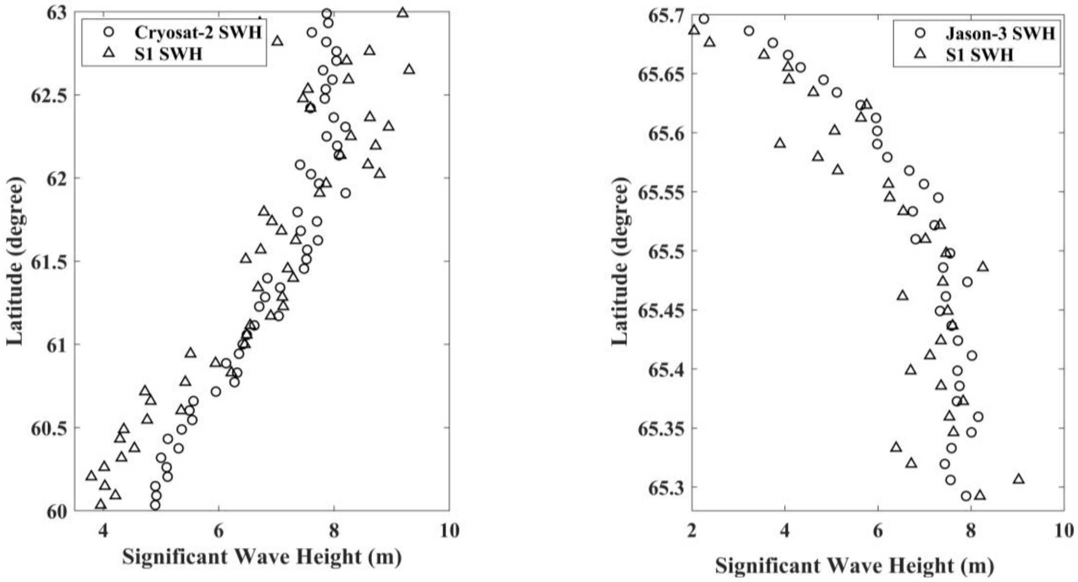

(e) (f)

Figure 10. (a) The S1 retrieved SWH of the case on 6 December 2018. The overlaid circles on the map represent the collocated CryoSat-2 SWH. The image ID of this case is S1A_EW_GRDM_1SDH_20181206T191419_20181206T191519_024909_02BE66_30DA. (c) ERA-5 reanalysis wind field at the synoptic time for case (a). (e) Scatter diagram of the comparison between the S1 SWH and CryoSat-2 SWH of (a). (b) The other case on November 2018 by S1B. The overlaid circles on the map represent the collocated Jason-3 SWH. The image ID of this case is S1B_EW_GRDM_1SDH_20181128T081302_20181128T081402_013802_019949_2ABC. (d) and (f) are the same as (c) and (e) but for the case presented in (b).

5 Comparison between the S1 retrieved SWH and CFOSAT/SWIM data

In this section, we compared the S1 retrieved SWH with the collocated CFOSAT/SWIM data acquired between August 2019 and May 2020. The SWIM measurements at nadir beam and 10° beam were used for a comparison with the S1 retrieved SWH. The S1 retrieved SWH and SWIM SWH were matched up in a temporal interval of 90 minutes. We first extracted the collocated S1 sub-images with dimensions of 70 km × 90 km, which is the same area as the wave cell of the 10° SWIM beam, and then we retrieved the SWH of these sub-images at a 2.56 km spatial resolution, finally, we computed the mean values of the retrieved SWH. Finally, we obtained 32,403 collocations between the data from S1 and the SWIM nadir beam and 1,283 collocations between the data from S1 and the SWIM 10° beam.

Fig. 11(a) shows the comparison between the S1 retrieved SWH and the collocated SWIM SWH at nadir. The bias is 0.15 m, the RMSE is 0.60 m and the SI is 18.98%, which are similar to the comparison with the RA SWH, as presented in Fig. 9 (c). Fig. 11 (a) also reveals that the S1 retrieved SWH is close to the SWIM nadir SWH when SWH is lower than approximately 5 m, but when SWH is above 6 m, the former is lower than the latter by approximately 0.84 m. The comparisons presented by Hauser et al. (2020) also suggested that the SWIM nadir SWH is at least 0.5 m higher than the ECMWF model SWH when the SWH is above 6 m. Fig.11 (b) and (c) show the comparisons between the S1 retrieved SWH and SWIM SWH at the 10° beam of the left and right tracks, respectively. These two comparisons suggest similar results in terms of the three statistical parameters, indicating that the SWIM SWH should have an identical performance on the left and right tracks of the 10° beam. For the comparisons above 6 m, one can find that the two data have large discrepancies. However, as there are only 56 collocations between the S1 and SWIM 10° beam SWH data above 6 m, the comparison for high sea state has limited significance. By excluding the data with SWH above 6 m from the comparisons, the three statistical parameters are all reduced with biases of -0.37 m and -0.36 m, of 0.74 m and 0.78 m, and SI of 20.41% and 20.44% for the left and right tracks, respectively. Hauser et al. (2020) also found that the SWIM SWH at the 10° beam is overestimated at SWH lower than 2 to 3 m and underestimated at larger wave heights with an RMSE of 0.26 m compared with the SWH provided by the MFWAM operational model.

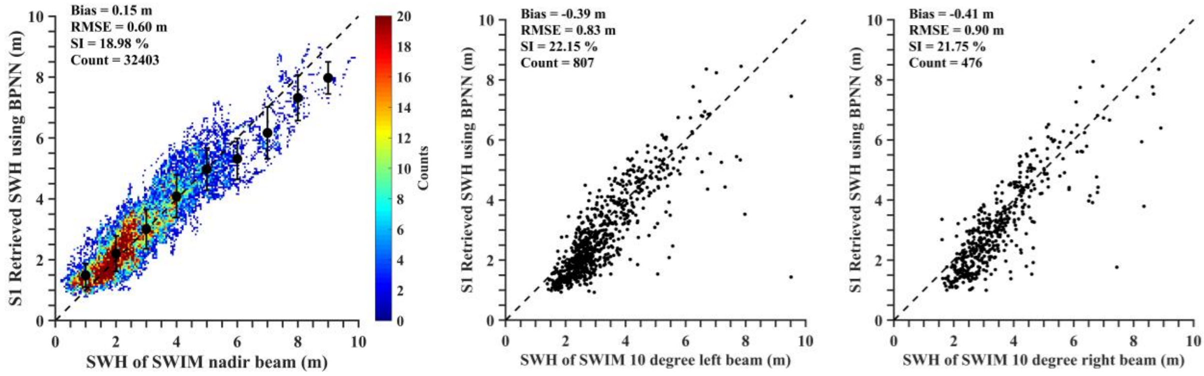

(a) (b) (c)

Figure 11. Comparisons between the S1 retrieved SWH and SWIM SWH at (a) nadir beam and at the 10° beam on the (b) left track and (c) right track.

Due to the nonlinear imaging mechanisms of ocean waves by spaceborne SAR, the retrievals of two-dimensional wave spectra and sea state parameters may suffer problems for short waves or azimuthal-traveling waves. The two-dimensional ocean wave information available from the SWIM sensor provides a unique opportunity to verify whether the SAR retrievals of sea state parameters depend on the wavelength and wave direction. Fig. 12 (a) and (b) show the differences between the S1 retrievals and SWIM SWH at the 10° beam (with a total of 1,283 data pairs by combining the collocations with the left and right SWIM tracks) varying with the dominant wavelength and azimuth wave direction (i.e., the dominant wave direction relative to the S1 azimuth direction) of SWIM. The step sizes of the histograms are 40 m for the dominant wavelength and 10° for the azimuth wave direction, respectively. The overlaid error bars represent the mean absolute bias and its standard deviation.

Fig. 12 (a) indicates that the S1 collocations with the 10° SWIM beam data are concentrated on the sea states with dominant wavelength less than 300 m. In this range, the mean absolute SWH bias is less than 0.70 m with limited fluctuations, and moreover, it is not found that the bias increases for the retrievals of waves with a relatively short wavelength, e.g., less than 100 m. With an increasing dominant wavelength, both the bias and the standard deviation increase, which is slightly different from our expectation, as SAR is generally considered suitable for the retrievals of ocean waves with long wavelength. However, the large bias (>0.5 m) obtained for data with a long wavelength (>300 m) may also attribute to quite less amount of collocated data pairs, accounting for only 5.79% of the total number of collocated data pairs.

Interestingly, the collocations between the S1 and 10° SWIM beam data are concentrated mainly on the sea states with azimuthal wave direction between 0° and 45° and between 135° and 180°, namely, close to the SAR flight direction. The biases for the collocated data in these two wave directions ranges are generally between 0.50 m and 0.75 m, and moreover, they are quite stable with no dependence on wave traveling directions. For the collocation data pairs with azimuthal wave traveling direction between approximately 60° and 120°, the biases are relatively large, generally larger than 0.75 m, and the fluctuations are quite distinct. These large biases may also be attributed to the smaller amount of collocated data with azimuthal wave directions in this range, accounting for only 4.89% of the total number of collocated data pairs.

These two comparisons suggest that the S1 retrieved SWH based on the proposed BPNN model tends to be independent on the wavelength and azimuth wave direction, while more collocations need to be collected in the future to draw a more reliable conclusion.

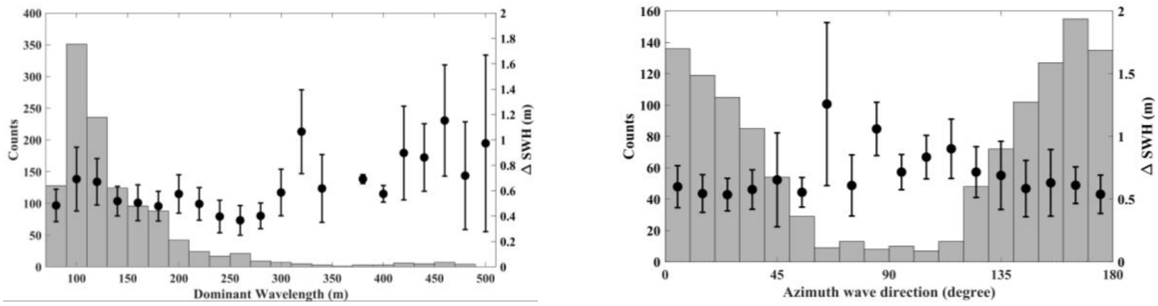

(a) (b)

Figure 12 Variation in ΔSWH with the (a) dominant wavelength and (b) azimuth wave direction provided by the 10° SWIM beam.

We further presented a case to compare the S1 retrieved SWH with the SWIM data in the Arctic MIZ. Three consecutive S1 EW images were acquired over the east of Greenland from 18:01 to 18:03 UTC on 26 February 2020. Fig. 13 (a) shows the S1 retrieved SWH of this case, in which the gray area represents sea-ice covered area based on the IMS data. The overlaid circles represent the SWIM nadir SWH observations, while the squares to the left and right of the track of circles are the SWH by SWIM at the 10° beam. The black arrows on the squares reflect the dominant wave direction derived from the SWIM data. The SWIM data were acquired at 18:38 UTC, 37 minutes later than the S1 acquisitions. From the northwest to the southeast, the SWH shows a trend of increasing and then decreasing, reaching a peak value of approximately 6 m at 66°N. Fig. 13 (b) is the sea surface wind field provided by the scatterometer onboard CFOSAT obtained at the same acquisition time as the SWIM data presented in Fig. 13 (a). The wind speed rises from 10 m/s to nearly 20 m/s and blows to the southwest, then decreases to 7-8 m/s with wind direction turning from southwest to southeast.

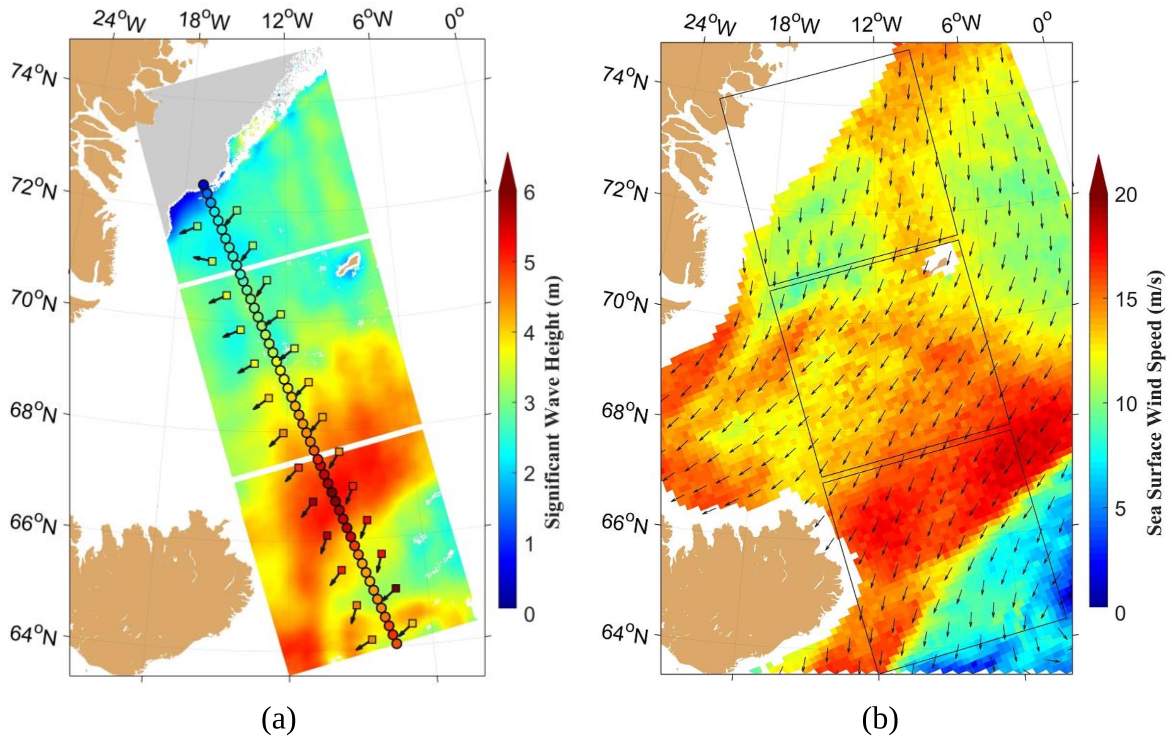

Figure 13 (a) S1 retrieved SWH map (background) with collocated SWIM SWH at nadir (circles) and at the left and right 10° beam tracks (squares). The arrows on the squares indicate the dominant wave directions. (b) Corresponding sea surface wind field by the scatterometer onboard CFOSAT. The ID of the three SAR images are S1A_EW_GRDM_1SDH_20200226T180128_20200226T180232_031427_039E37_EE97, S1A_EW_GRDM_1SDH_20200226T180232_20200226T180332_031427_039E37_559A, and S1A_EW_GRDM_1SDH_20200226T180332_20200226T180432_031427_039E37_19C3.

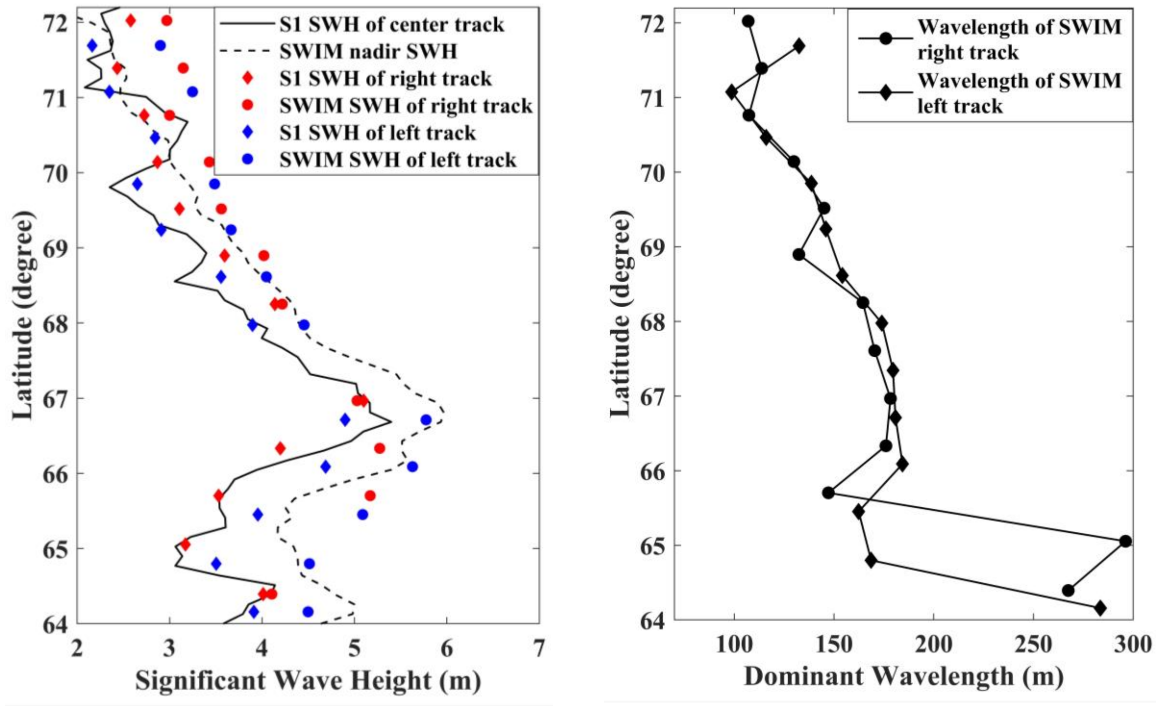

(a) (b)

Figure 14. (a) Statistical graph of the S1 SWH on three tracks and the collocated SWIM SWH. (b) Line chart of the dominant wavelength provided by the 10° SWIM beam on two tracks.

Fig. 14 (a) shows comparisons among the S1 retrieved SWH and the collocated SWIM SWH at nadir and the 10° beam (right and left tracks). The dashed line shows the SWIM SWH at nadir, and the solid line represents the collocated S1 retrieved SWH at the SWIM nadir track. The red and blue circle symbols represent the SWIM SWH on the right and left tracks of the 10° beam, respectively. The diamonds with the same color are the collocated S1 retrieved SWH. In the region between approximately 64°N and 70°N, the SWH varies from 3 m to 6 m, and the SWIM SWH at nadir shows a similar spatial variation as the S1 retrievals. However, the SWIM SWH is systematically higher than the collocated S1 SWH by approximately 0.57 m.

The SWIM SWH of the left and right tracks at the 10° beam are also higher than the collocated S1 retrieved SWH by 0.80 m and 0.55 m on average, respectively. Fig. 14 (b) shows the dominant wavelength provided by SWIM at the 10° beam. The symbols of diamond and circle represent the results for the left and right tracks, respectively. From 72°N to 66°N, the dominant wavelength increases gradually from 107 m to 184 m. This increasing trend of wavelength is also consistent with the increasing trend of SWH, indicating the development of an ocean wave field. After a small decrease at 66°N, the dominant wavelength sharply increases to nearly 300 m, indicating a swell-dominated sea state.

To further investigate this case, we chose three two-dimensional wave spectra provided by SWIM at the 10° beam for demonstration, as shown in Fig. 15. Their integral wave parameters and the collocated S1 retrieved SWH are listed in Table 3. Fig. 15 (a) shows the sea state involving both wind sea (with a peak wavelength of approximately 152 m) and swell (455 m); consequently, the dominant wavelength in region 1 is 145 m. The SWH for this region by S1 and SWIM are similar with values of 3.11 m and 3.56 m, respectively. In region 2 (Fig. 15 (b)), the sea state developed further, with longer dominant wavelength of 184 m compared with the sea state at region 1. With sea state increasing, the difference between the S1 retrieval and SWIM SWH increases to approximately 1.0 m (4.69 m vs. 5.63 m). The two-dimensional wave spectrum presented in Fig. 15 (c) suggests that the sea state in region 3 is swell-dominated with a wavelength of 283 m. This swell system should have developed from windsea at previous times, as its wave direction (60.68°, going to) is approximately 45° from the local wind direction (15°). In addition to this dominant swell peak, there is another weak peak with a wavelength of approximately 200 m and a wave direction of approximately 15°, consistent with the sea surface wind direction, which may indicate a young swell just leaving the generation area. For region 3, although its wave height is lower than that of region 2, the SWIM SWH is still higher than the S1 retrieved SWH by 0.6 m.

This case reveals complicated sea state conditions with a mixture of windsea and swell systems. Swells developed in previous times propagated further, and they coexisted with locally generated windsea or young swells, as the high wind field also continuously moved. The SWIM nadir SWH shows better agreement with the S1 retrievals than the data at the 10° beam in this case. Although the SWIM SWH at both the nadir beam and the 10° beam are higher than the S1 retrievals, the differences between the SWIM nadir and S1 retrieved SWH seem to be systematic, while the differences between the 10° beam and S1 retrieved SWH are significantly variable.

Table 3. Parameters and collocated S1 SWH of the three wave spectra in Fig. 15.

Wave spectrum	1	2	3
Longitude	11.60°W	10.26°W	8.54°W
Latitude	69.52°N	66.09°N	64.16°N
S1 retrieved SWH	3.11 m	4.69 m	3.91 m
SWIM SWH	3.56 m	5.63 m	4.50 m
SWIM wavelength	145.04 m	184.36 m	283.53 m
SWIM wave direction	53.93°	20.64°	60.68°
Sea surface wind speed (CFOSAT/scatterometer)	13.80 m/s	16.58 m/s	8.21 m/s

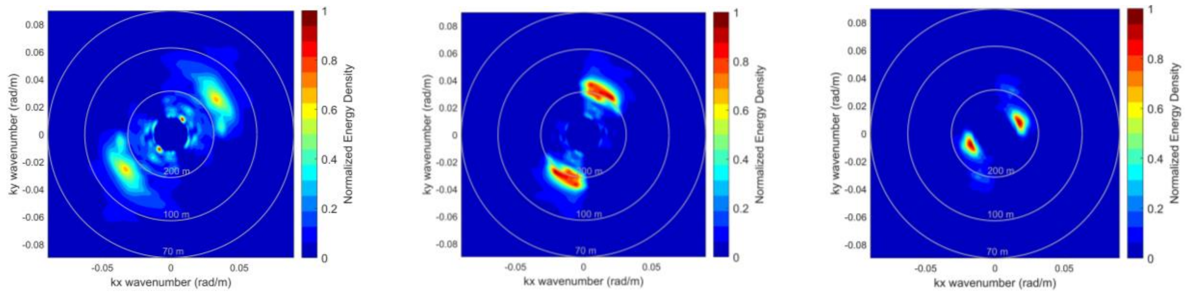

(a) (b) (c)

Figure 15. Two-dimensional wave spectrum provided by the 10° SWIM beam in three regions: 69.52°N/11.60°W, 66.09°N/10.26°W and 64.16°N/8.54°W. The corresponding integral wave parameters are listed in Table 3. All the wave spectra are oriented with respect to true north (up represents north).

6. Summary and conclusions

The interaction between ocean dynamics and sea ice in the Arctic starts to draw more attention due to the rapid decrease in the sea ice extent. As the basis of ocean dynamics, accurate measurements of ocean wave parameters by remote sensing data in the MIZ are highly desirable. S1A and S1B have extensively acquired spaceborne SAR data at both high spatial resolution and large spatial coverage in the Arctic, providing unique advantages in the acquisition of sea state information in the Arctic MIZ. Therefore, in this study, we focus on developing a practical method to derive sea state parameter of the SWH from S1 SAR data, which can be used further to study the interaction between ocean waves and sea ice.

Previous studies have demonstrated that empirical algorithms are practical to derive integral wave parameters, e.g., the SWH and mean wave period, from SAR data than traditional nonlinear inversions, as these algorithms do not need a priori information. In this study, we adopted the idea of previous SAR-ocean wave empirical algorithms, but incorporated these ideas into a BPNN model. BPNN is good at fitting nonlinear relationships between inputs and outputs. There are 23 parameters derived from SAR data used as inputs into the BPNN model, and the sole output parameter is the collocated RA SWH. Based on 126,128 collocated data pairs of S1 EW and four RA missions in the Arctic, we developed a BPNN model for SWH retrievals. The determined BPNN based on numbers of experiments has four hidden layers and the nodes of the hidden layers is 30, 20, 10 and 5, respectively.

By comparing the S1 retrieved SWH with the RA SWH based on the testing dataset, we achieved a good result with a bias of 0.02 m, an RMSE of 0.63 m and an SI of 21.07%. However, we also found that the retrievals underestimate the sea state for SWH higher than approximately 4 m. This problem cannot be solved by changing the structure of the BPNN model, e.g., adding more hidden layers and nodes, or adding more training data (in fact more than 1 million training samples were employed herein). Our solution was to arbitrarily increase the proportion of training samples in high sea state by duplicating the original collocated data pairs. This approach increases the weights of training samples of high sea state during the BPNN training process. Although the bias of the retrievals based on the adjusted training dataset is higher than that of the results based on the original training dataset (0.17 m vs. 0.02 m), the underestimation of the S1 retrievals in high sea state (above 5 m) is significantly reduced. In particular, an increasing underestimation trend with sea state is not observed. We recently used the same way to solve the underestimation of sea surface wind speed retrievals by the same S1 EW data in HH polarization (Li et al., 2020).

We further compared the S1 retrieved SWH with the SWIM SWH at nadir and the 10° beam. The comparison at nadir yields a bias of 0.15 m, an RMSE of 0.60 m and an SI of 18.98%, which is similar to the comparison with the RA SWH. This result is also consistent with the comparisons achieved by Hauser et al. (2020), the CFOSAT/SWIM development team, which indicates that the S1 retrievals should be of relatively good quality. However, a comparison of the same dataset of S1 retrievals with the SWIM SWH at the 10° beam (on either the left track or the right track) shows that the SWIM SWH is much higher than S1 retrievals with a bias of approximately 0.4 m and an RMSE of 0.90 m. Moreover, both the statistical analysis and the case study indicate that the differences between the 10° SWIM beam SWH and the S1 retrievals vary considerably. Although the difference between the S1 retrieved SWH and the SWIM SWH at the 10° beam is rather large, the S1 retrieved SWH is independent of the dominant wavelength and azimuthal wave direction, indicating that the proposed BPNN model can yield stable retrievals of SWH by S1 data.

These comparisons suggest that the quality of SWIM wave data should be improved in the future. In October 2020, the SWIM development team announced that the current modulation transfer function (MTF) has been adjusted and the reprocessing of all SWIM data since the beginning of the mission will be triggered. We expect better SWIM data for further research.

On the other hand, the S1 retrievals based on the proposed BPNN also have room for improvement. One issue that remains unresolved is that it is difficult to retrieve correctly SWH less than 1.5 m due to the insensitivity of SAR signals to low sea states. SAR cross-polarization data are less saturated with high wind compared with co-polarization data (Monaldo, et al., 2017). We recently developed a robust method for denoising S1 HV-polarized data (Sun & Li, 2020), therefore, we expect to obtain better results for high sea states by combining data in both HH and HV polarization. Furthermore, to date, only integral wave parameter of SWH has been retrieved based on a neural network; hence, it might be possible to retrieve two-dimensional wave spectra based on deep learning methods without through the complicated nonlinear inversions.

The MATLAB code to retrieve SWH by the S1 data in HH polarization using the proposed method was published in Zenodo for public sharing (Wu, 2020).

Acknowledgments: The S1 SAR data are downloaded from the Copernicus data hub (https://scihub.copernicus.eu/), the CryoSat-2 data are downloaded from the CryoSat-2 Science Server (https://science-pds.cryosat.esa.int/), the Jason-2/3 data and SARAL data are downloaded from EUMETSAT (https://archive.eumetsat.int/), and the CFOSAT SWIM data are downloaded from AVISO (https://aviso-data-center.cnes.fr). Use of the reference data of IMS data (https://www.natice.noaa.gov/ims/), the ERA-5 data (https://cds.climate.copernicus.eu/cdsapp#!/home) and the CFOSAT scatterometer data (https://osdds.nsoas.org.cn) is also acknowledged. This work was supported in part by the National Key Research and Development Project (2018YFC1407100) China.

Appendix: Estimation of the SAR Image Spectrum

The SAR image spectrum is estimated by computing the image periodogram with a 2-D FFT algorithm. The idea is to divide an image with 256 × 256 samples into 2 × 2 sub-images with 128 × 128 samples and then to compute the FFT of each sub-image and obtain the power spectral density. Finally, the SAR image spectrum is acquired by computing the average of 4 power spectral densities.

The 2-D FFT is applied to every normalized sub-image G:

$$F_G = fft_{128}(G)\#(A1)$$

where 128 represents the size of every sub-image. The power density spectrum is denoted by P_S:

$$P_S = (F_G)^2\#(A2)$$

Then, summing the four power density spectra and averaging them, the entire SAR image spectrum P is given by:

$$P = \frac{1}{2 \times 2}\sum P_S\,\#(A3)$$

The power density spectrum needs to be normalized to ensure that the integral of the image in the frequency domain is equal to that in the spatial domain. The normalized image spectrum is denoted as $\bar{P}$:

$$\bar{P} = P * \left(\sum P * dk_x * dk_y\right)^{-1}\#(A4)$$

where dk_x and dk_y is the wavenumber spacing in the SAR image range and azimuth direction, respectively, given by:

$$dk_x = 2\pi/(128 * d_x)\,\#(A5)$$

$$dk_y = 2\pi/\left(128 * d_y\right)\#(A6)$$

where d_x and d_y is the pixel spacing (in meters) of the SAR image, and in this study, both d_x and d_y are equal to 40 m.

The SAR spectral parameters are the scalar product of SAR image spectrum $\bar{P}$ and orthonormal functions:

$$S = \sum \bar{P}\left(k_x, k_y\right)\overline{h_i}\left(k_x, k_y\right) dk_x dk_y \ \#(A7)$$

where $1 \le i \le n_\varphi n_k$ and $\overline{h_i}$ are the orthonormal functions, which are described in (A8).

The orthonormal functions $\overline{h_{ij}}$ are used to extract the image spectral parameters in wavenumber *k* and angular φ dimensions and are composed of Gegenbauer polynomials $g_i(\alpha_k)$ and harmonic functions $f_j(\alpha_\varphi)$:

$$\overline{h_{ij}}\left(\alpha_k, \alpha_\varphi\right) = \eta\left(k_x, k_y\right) g_i(\alpha_k) f_j\left(\alpha_\varphi\right), 1 \le i \le n_k, 1 \le j \le n_\varphi \#(A8)$$

where $\eta\left(k_x, k_y\right)$ is the elliptical area. The four Gegenbauer polynomials are:

$$g_1(\alpha_k) = \frac{1}{2}\sqrt{3}\sqrt{1 - \alpha_k^2} \#(A9)$$

$$g_2(\alpha_k) = \frac{1}{2}\sqrt{15}\alpha_k\sqrt{1 - \alpha_k^2} \#(A10)$$

$$g_3(\alpha_k) = \frac{1}{4}\sqrt{\frac{7}{6}}(15\alpha_k^2 - 3)\sqrt{1 - \alpha_k^2} \#(A11)$$

$$g_4(\alpha_k) = \frac{1}{4}\sqrt{\frac{9}{10}}(35\alpha_k^3 - 15\alpha_k^2)\sqrt{1 - \alpha_k^2} \#(A12)$$

The five harmonic functions are:

$$f_1\left(\alpha_\varphi\right) = \sqrt{1/\pi} \ \#(A13)$$

$$f_2\left(\alpha_\varphi\right) = \sqrt{2/\pi} \sin\left(2\alpha_\varphi\right) \#(A14)$$

$$f_3\left(\alpha_\varphi\right) = \sqrt{2/\pi} \cos\left(2\alpha_\varphi\right) \#(A15)$$

$$f_4\left(\alpha_\varphi\right) = \sqrt{2/\pi} \sin\left(4\alpha_\varphi\right) \#(A16)$$

$$f_5\left(\alpha_\varphi\right) = \sqrt{2/\pi} \cos\left(4\alpha_\varphi\right) \#(A17)$$

α_k and α_φ define the integration area A in the wavenumber domain of the SAR image spectra and are defined as:

$$\alpha_k\left(k_x, k_y\right) = 2\frac{\log\sqrt{a_1 k_x^4 + a_2 k_x^2 + k_y^2} - \log k_{min}}{\log k_{max} - \log k_{min}} - 1\#(A18)$$

$$\alpha_{\varphi}(k_x, k_y) = \arctan(k_y, k_x) \#(A19)$$

The two parameters a_1 and a_2 in (A18) are:

$$a_1 = \frac{\gamma^2 - \gamma^4}{\gamma^2 k_{min}^2 - k_{max}^2} \#(A20)$$

$$a_2 = \frac{k_{max}^2 - \gamma^4 k_{min}^2}{k_{max}^2 - \gamma^2 k_{min}^2} \#(A21)$$

where $\gamma = 2$, which describes the velocity bunching effect in the SAR imaging process. k_{max} and k_{min} are the maximum and minimum wavenumber in the integration area, respectively:

$$k_{max} = \frac{2\pi}{60m} \#(A22)$$

$$k_{min} = \frac{2\pi}{624m} \#(A23)$$

The weight function $\eta(k_x, k_y)$ in (A8) is defined as:

$$\eta(k_x, k_y) = \left(\frac{2(a_1 k_x^4 + a_2 k_x^2 + k_y^2)}{(k_x^2 + k_y^2)(a_1 k_x^4 + a_2 k_x^2 + k_y^2)(\log k_{max} - \log k_{min})} \right)^{\frac{1}{2}} \#(A24)$$

The 20 orthonormal functions are visualized in Fig. A1, in which the gray values have a linear scaling between -25 (black) and 25 (white).

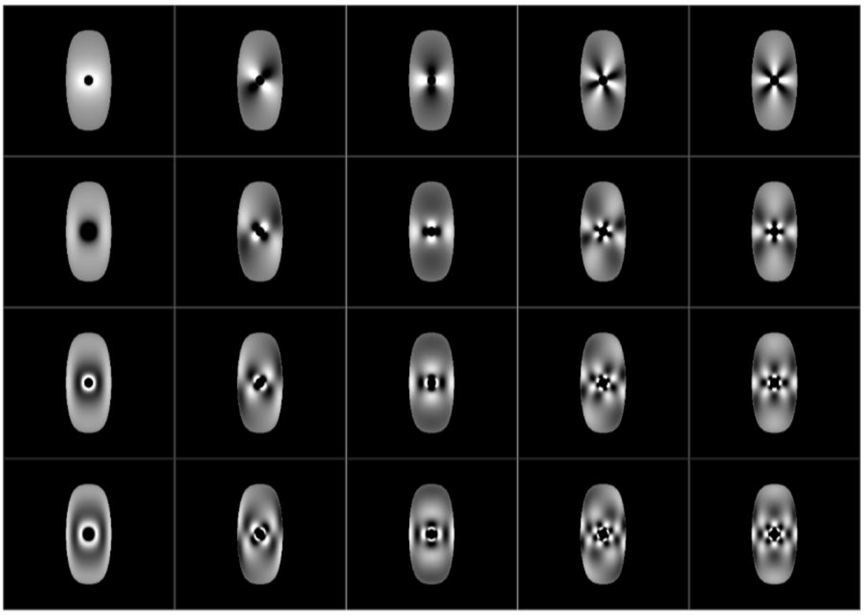

Figure A1. Orthonormal functions used to extract ocean wave information from the SAR image spectrum for $n_\varphi = 4$ and $n_k = 5$. The gray values have a linear scaling between -25 (black) and 25 (white). Values below -25 or above 25 m appear as black or white, respectively.

References

Alpers, W. R., Ross, D. B., & Rufenach, C. L. (1981). On the detectability of ocean surface waves by real and synthetic aperture radar. *Journal of Geophysical Research, 86*(C7). doi:10.1029/JC086iC07p06481

Ardhuin, F., Stopa, J. E., Chapron, B., Collard, F., Husson, R., Jensen, R. E., et al. (2019). Observing Sea States. *Frontiers in Marine Science, 6*. doi:10.3389/fmars.2019.00124

Asplin, M. G., Galley, R., Barber, D. G., & Prinsenberg, S. (2012). Fracture of summer perennial sea ice by ocean swell as a result of Arctic storms. *Journal of Geophysical Research: Oceans, 117*(C6), doi:10.1029/2011JC007221.

Bruck, M., & Lehner, S. (2013). Coastal wave field extraction using TerraSAR-X data. *Journal of Applied Remote Sensing, 7*(1), 073694, doi:10.1117/1.JRS.7.073694.

Cavalieri, D. J., & Parkinson, C. L. (2012). Arctic sea ice variability and trends, 1979–2010. *The Cryosphere, 6*(4), 881-889. doi:10.5194/tc-6-881-2012

Comiso, J. C., Meier, W. N., & Gersten, R. (2017). Variability and trends in the Arctic Sea ice cover: Results from different techniques. *Journal of Geophysical Research:Oceans, 122*(8), 6883-6900, doi:10.1002/2017JC012768.

Ding, Y., Zuo, J., Shao, W., Shi, J., Yuan, X., Sun, J., et al. (2019). Wave parameters retrieval for dual-polarization C-band synthetic aperture radar using a theoretical-based algorithm under cyclonic conditions. *Acta Oceanologica Sinica, 38*(5), 21-31. doi:10.1007/s13131-019-1438-y

Engen, G., & Johnsen, H. (1995). SAR-ocean wave inversion using image cross spectra. *IEEE Transactions on Geoscience Remote Sensing, 33*(4), 1047-1056, doi: 10.1109/36.406690

Gao, D., Liu, Y., Meng, J., Jia, Y., & Fan, C. (2018). Estimating significant wave height from SAR imagery based on an SVM regression model. *Acta Oceanologica Sinica, 37*(3), 103-110. doi:10.1007/s13131-018-1203-7

Hasselmann, K., & Hasselmann, S. (1991). On the nonlinear mapping of an ocean wave spectrum into a synthetic aperture radar image spectrum and its inversion. *Journal of Geophysical Research, 96*(C6). doi:10.1029/91jc00302

Hasselmann, S., Brüning, C., Hasselmann, K., & Heimbach, P. (1996). An improved algorithm for the retrieval of ocean wave spectra from synthetic aperture radar image spectra. *Journal of Geophysical Research: Oceans, 101*(C7), 16615-16629. doi:10.1029/96jc00798

Hauser, D., Tourain, C., Hermozo, L., Alraddawi, D., & Tran, N. T. (2020). New Observations From the SWIM Radar On-Board CFOSAT: Instrument Validation and Ocean Wave Measurement Assessment. *IEEE Transactions on Geoscience and Remote Sensing,* doi: 10.1109/TGRS.2020.2994372.

Hong, D. B., & Yang, C. S. (2018). Automatic discrimination approach of sea ice in the Arctic Ocean using Sentinel-1 Extra Wide Swath dual-polarized SAR data. *International Journal of Remote Sensing, 39*(13), 4469-4483.

Kumar, N. K., Savitha, R., & Mamun, A. A. (2018). Ocean wave height prediction using ensemble of Extreme Learning Machine. *Neurocomputing, 277*, 12-20. doi:10.1016/j.neucom.2017.03.092

Lehner, S., & Ocampo-Torres, F. J. (2003). The SAR measurement of ocean waves: wave session whitepaper *Torres*, *565*.

Li, X. -M. (2016). A new insight from space into swell propagation and crossing in the global oceans. *Geophysical Research Letters, 43*(10), 5202-5209, doi:10.1002/2016gl068702

Li, X. -M., & Huang, B. Q. (2020). A global sea state dataset from spaceborne synthetic aperture radar wave mode data. *Scientific Data, 7*(1), 261, doi:10.20944/preprints202001.0200.v1

Li, X. -M., Lehner, S., & Bruns, T. (2011). Ocean Wave Integral Parameter Measurements Using Envisat ASAR Wave Mode Data. *IEEE Transactions on Geoscience and Remote Sensing, 49*(1), 155-174, doi:10.1109/Tgrs.2010.2052364

Li, X. -M., Qin, T. T., & Wu, K. (2020). Retrieval of Sea Surface Wind Speed from Spaceborne SAR over the Arctic Marginal Ice Zone with a Neural Network. *Remote Sensing, 12*(20). doi:10.3390/rs12203291

Li, X. -M., Sun, Y., & Zhang, Q. (2020). Extraction of Sea Ice Cover by Sentinel-1 SAR Based on Support Vector Machine With Unsupervised Generation of Training Data. *IEEE Transactions on Geoscience Remote Sensing*, doi:10.1109/TGRS.2020.3007789

Liu, J. , Lin, W. , Dong, X. , Lang, S. , & Jiang, X. . (2020). First results from the rotating fan beam scatterometer onboard CFOSAT. *IEEE Transactions on Geoscience and Remote Sensing,* doi: 10.1109/TGRS.2020.2990708

Mastenbroek, C., & De Valk, C. F. (2000). A semiparametric algorithm to retrieve ocean wave spectra from synthetic aperture radar. *Journal of Geophysical Research:Oceans, 105*(C2), 3497-3516. doi: 10.1029/1999jc900282

Monaldo, F. M., Jackson, C, & Li, X. (2017). On the use of Sentinel-1 cross-polarization imagery for wind speed retrieval. Paper presentes at 2017 IEEE International Geoscience and Remote Sensing Symposium (IGARSS), Fort Worth, America.

Nose, T., Waseda, T., Kodaira, T., & Inoue, J. (2020). Satellite-retrieved sea ice concentration uncertainty and its effect on modelling wave evolution in marginal ice zones. *The Cryosphere, 14*(6), 2029-2052. doi:10.5194/tc-14-2029-2020

Pramudya, F. S., Pan, J. Y., & Devlin, A. T. (2019). Estimation of Significant Wave Height of Near-Range Traveling Ocean Waves Using Sentinel-1 SAR Images. *IEEE Journal of Selected Topics in Applied Earth Observations and Remote Sensing, 12*(4), 1067-1075. doi:10.1109/Jstars.2019.2902566

Rumelhart, D. E., Hinton, G. E., & Williams, R. J. (1986). Learning representations by back-propagating errors. *Nature, 323*(6088), 533-536.

Schulz-Stellenfleth, J. (2005). A parametric scheme for the retrieval of two-dimensional ocean wave spectra from synthetic aperture radar look cross spectra. *Journal of Geophysical Research, 110*(C5). doi:10.1029/2004jc002822

Schulz-Stellenfleth, J., König, T., & Lehner, S. (2007). An empirical approach for the retrieval of integral ocean wave parameters from synthetic aperture radar data. *Journal of Geophysical Research, 112*(C3). doi:10.1029/2006jc003970

Schulz-Stellenfleth, J., & Lehner, S. (2004). Measurement of 2-D Sea Surface Elevation Fields Using Complex Synthetic Aperture Radar Data. *IEEE Transactions on Geoscience and Remote Sensing, 42*(6), 1149-1160. doi:10.1109/tgrs.2004.826811

Shao, W., Ding, Y. Y., Li, J., Gou, S., Nunziata, F., Yuan, X., et al. (2019). Wave Retrieval Under Typhoon Conditions Using a Machine Learning Method Applied to Gaofen-3 SAR Imagery. *Canadian Journal of Remote Sensing, 45*(6), 723-732. doi:10.1080/07038992.2019.1683444

Shao, W., Hu, Y. Y., Zheng, G., Cai, L. N., & Zou, J. C. (2019). Sea State Parameters Retrieval from Cross-polarization Gaofen-3 SAR Data. *Advances in Space Research, 65*(3), 1025-1034. doi: 10.1016/j.asr.2019.10.034.

Soldal, I., Dierking, W., Korosov, A., & Marino, A. (2019). Automatic Detection of Small Icebergs in Fast Ice Using Satellite Wide-Swath SAR Images. *Remote Sensing, 11*(7), 806. doi: 10.3390/rs11070806

Stopa, J. E., Ardhuin, F., Thomson, J., Smith, M. M., Kohout, A., Doble, M., et al. (2018). Wave Attenuation Through an Arctic Marginal Ice Zone on 12 October 2015: 1. Measurement of Wave Spectra and Ice Features From Sentinel 1A. *Journal of Geophysical Research: Oceans, 123*(5), 3619-3634. doi:10.1029/2018jc013791

Stopa, J. E., & Mouche, A. (2017). Significant wave heights from Sentinel-1 SAR: Validation and applications. *Journal of Geophysical Research: Oceans, 122*(3), 1827-1848. doi:10.1002/2016jc012364

Strong, C., & Rigor, I. G. (2013). Arctic marginal ice zone trending wider in summer and narrower in winter. *Geophysical Research Letters, 40*(18), 4864-4868. doi:10.1002/grl.50928

Sun, Y., & Li, X. -M. (2020). Denoising sentinel-1 extra-wide mode cross-polarization images over sea ice. *IEEE Transactions on Geoscience and Remote Sensing*, doi:10.1109/TGRS.2020.3005831

Thomson, J., & Rogers, W. E. (2014). Swell and sea in the emerging Arctic Ocean. *Geophysical Research Letters, 41*(9), 3136-3140.

Ulaby, F. T., Long, D. G., Blackwell, W., Elachi, C., & Zebker, H. (2015). *Microwave radar and radiometric remote sensing*: The University of Michigan Press.

Valenzuela, G. R. (1978). Theories for the interaction of electromagnetic and oceanic waves — A review. *Boundary-Layer Meteorology, 13*(1-4), 61-85.

Xue, S., Geng, X., Yan, X. H., Xie, T., & Yu, Q. (2018). Significant wave height retrieval from Sentinel-1 SAR imagery by convolutional neural network. *Journal of Oceanography*, 1-13, doi:10.1007/s10872-020-00557-3.

Zhu, J., Dong, X., Lin, W., & Zhu, D. (2015). A Preliminary Study of the Calibration for the Rotating Fan-Beam Scatterometer on CFOSAT. *IEEE Journal of Selected Topics in Applied Earth Observations and Remote Sensing, 8*(2), 460-470. doi:10.1109/jstars.2014.2333241

Wu, K. (2020). MATLAB code for significant wave height retrieval by Sentinel-1 SAR data in HH polarization. *Zenodo*, http://doi.org/10.5281/zenodo.4158824